JACS
JOURNAL OF THE AMERICAN CHEMICAL SOCIETY
pubs.acs.org/JACS
Article

High-Energy, High-Power Sodium-Ion Batteries from a Layered Organic Cathode

Tianyang Chen, Jiande Wang, Bowen Tan, Kimberly J. Zhang, Harish Banda, Yugang Zhang, Dong-Ha Kim, and Mircea Dincă*

Cite This: https://doi.org/10.1021/jacs.4c17713
Read Online

ABSTRACT: Sodium-ion batteries (SIBs) attract significant attention due to their potential as an alternative energy storage solution, yet challenges persist due to the limited energy density of existing cathode materials. In principle, redox-active organic materials can tackle this challenge because of their high theoretical energy densities. However, electrode-level energy densities of organic electrodes are compromised due to their poor electron/ion transport and severe dissolution. Here, we report the use of a low-bandgap, conductive, and highly insoluble layered metal-free cathode material for SIBs. It exhibits a high theoretical capacity of 355 mAh g^{-1} per formula unit, enabled by a four-electron redox process, and achieves an electrode-level energy density of 606 Wh $kg^{-1}_{electrode}$ (90 wt % active material) along with excellent cycling stability. It allows for facile two-dimensional Na^+ diffusion, which enables a high intrinsic rate capability. Growth of the active cathode material in the presence of as little as 2 wt % carboxyl-functionalized carbon nanotubes improves charge transport and charge transfer kinetics and further enhances the power performance. Altogether, these allow the construction of SIB cells built from an affordable, sustainable organic small molecule, which provide a cathode energy density of 472 Wh $kg^{-1}_{electrode}$ when charging/discharging in 90 s and a top specific power of 31.6 kW $kg^{-1}_{electrode}$.

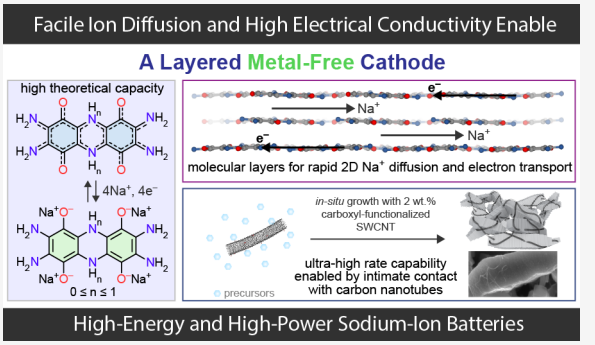

INTRODUCTION

Owing to sodium's widespread availability, sodium-ion batteries (SIBs) have attracted tremendous attention as a promising complementary technology to lithium-ion batteries (LIBs),[1] especially for stationary energy storage such as (micro)grids, data centers, and commercial-scale renewable energy systems. Cathode materials are pivotal to determining the performance of SIBs. Significant progress has been made with SIBs using various cathode materials, including layered transition metal oxides,[2] Prussian blue analogues,[3] and polyanionic compounds.[4] However, achieving both high energy density and high power density at the electrode level remains a major challenge.[5] While the former requires high specific capacity and high voltage, the latter demands facile ion and electron transport.

To overcome this challenge, redox-active organic electrode materials (OEMs), typically composed of earth-abundant elements like C, H, N, O, and S, have recently emerged as a promising solution, providing substantial opportunities due to their high theoretical specific capacity (e.g., >350 mAh g^{-1}) and moderate redox potential (1.5−3 V vs Na^+/Na).[6,7] These properties lead to a superior material-level energy density when compared to conventional inorganic cathode materials. However, 30 wt % conductive carbon is generally required to turn these pure cathode materials into functional electrode composites because traditional OEMs show inherently low electrical conductivity, often below 10^{-7} S m^{-1}.[8,9] Cycling OEM-based SIBs at high rates also requires fast Na^+ transport, which in turn imposes new additive requirements: larger amounts of conductive carbon (>40 wt %) or 20−30 wt % advanced carbon materials such as graphene and carbon nanotubes (CNTs) (Figure S1). This high additive requirement severely impairs the electrode-level energy density. Employing low-energy gap OEMs with higher electrical conductivity would alleviate part of the carbon additive requirement. With respect to ionic transport, there is not a clear correlation between structural/compositional features and Na-ion diffusion, but it has been observed that crystalline networks that allow facile two-dimensional (2D) diffusion pathways, such as *T*-Nb_2O_5,[10] enable rapid intercalation of metal ions.

Clearly, employing a crystalline OEM that is electrically conductive and has an ordered 2D structure that could allow for fast Na^+ intercalation may be expected to reduce the need for carbon additives. However, a third problem arises with

Received: December 11, 2024
Revised: January 22, 2025
Accepted: January 24, 2025

traditional OEMs: many materials in this class do not cycle well because they ultimately dissolve in the electrolyte. To prevent this, various additives are again employed. Alternative solutions that immobilize the active organic redox unit: polymerization,[11,12] framework construction,[13] and salinization[14,15] add significant "dead mass" that inevitably reduces the electrode-level energy and power densities (Figure S1). To this end, an ideal solution would be to a redox-active OEM that is intrinsically insoluble.

Here, we report the performance of a layered organic solid, bis-tetraaminobenzoquinone (TAQ) (Figure 1a), as cathode material in SIBs. TAQ displays high energy and power density at the electrode level. TAQ comprises strongly hydrogen-bonded molecular 2D layers that address all previous challenges with OEMs in SIBs: the layered structure leads to narrow electronic bandgap with high electrical conductivity,[16,17] it allows rapid intercalation and quasi-2D diffusion of Na^+ in-between layers, and the closely stacked 2D hydrogen bonding lattice essentially eliminates solubility. TAQ-based cathodes exhibit a reversible specific capacity that nears the theoretical value of 355 mAh g^{-1} per formula unit (Figure 1b), alongside fast charging/discharging capability, and long lifetime enabled by electrolyte optimization. Importantly, TAQ-based cathodes achieve a record high electrode-level energy density of 606 Wh $kg^{-1}_{electrode}$. *Operando* studies reveal small reversible crystal-structural changes of TAQ during cycling, confirming the structural integrity of TAQ due to robust intermolecular interactions.

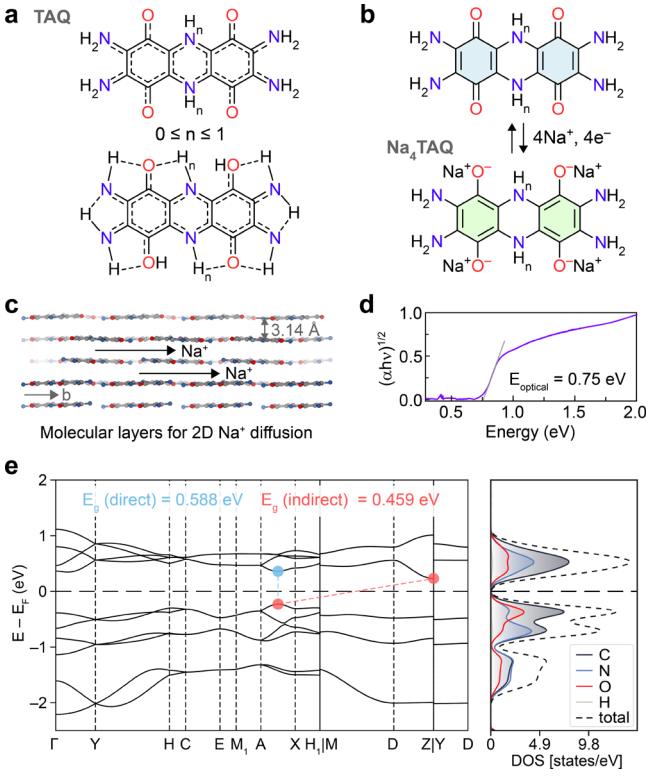

Figure 1. Structure and characterization of TAQ. (a) Molecular structure of TAQ, and its delocalized representation including hydrogen bonding and tautomerization. (b) Na^+ storage chemistry of TAQ. (c) The layered structure of TAQ with an interlayer distance of 3.14 Å. These molecular layers provide 2D diffusion pathways for Na^+. (d) Diffuse reflectance UV−vis−NIR spectrum of TAQ plotted in the Tauc coordinates, revealing an optical bandgap of 0.75 eV. (e) Band structure and projected density of states of TAQ.

Furthermore, electrode composite-level engineering through hydrogen-bonding assisted growth of TAQ crystals with carboxyl functionalized single-walled carbon nanotubes (cSWCNTs) produces composites comprising TAQ crystals mixed with as little as ∼2 wt % cSWCNTs. Such composites exhibit significantly improved electrical conductivity due to close contact between TAQ crystallites and cSWCNTs. The TAQ-CNT composite electrodes exhibit ultrahigh rate capability, delivering 150 mAh g^{-1} at 20 A g^{-1} with an electrode-level power density of 31.6 kW $kg^{-1}_{electrode}$.

RESULTS AND DISCUSSION

Characterization of TAQ. As previously reported,[16,17] TAQ is isolated as microcrystals wherein TAQ molecules are held by pervasive hydrogen bonding between carbonyl and amino groups into closely π-stacked 2D molecular layers (Figures 1c and S2−S6). The stacking of these layers follows a donor−acceptor manner, where electron-deficient carbon atoms pertaining to carbonyl groups are situated directly above electron-rich oxygen atoms or amino-N atoms (Figure S4d), leading to a short interlayer distance of 3.14 Å that is rarely observed in pure organic materials.[18,19] Previously described electron diffraction analysis by us identified only non-hydrogen atoms in the crystal structure;[16] whereas the central C−N bond lengths (∼1.41 Å) point to a dihydropyrazine formulation for the central ring, an oxidized ring (i.e., pyrazine) has also been proposed previously.[20] We also demonstrated previously that TAQ contains organic radicals (∼3 mol %) likely due to the partial oxidation of the central dihydropyrazine ring which removes H·.[17] As such, TAQ is best described as any composition within the continuum $C_{12}H_{8+2n}N_6O_4$ ($0 \le n \le 1$) depending on the degree of oxidation of the central dihydropyrazine ring. Importantly, because the hydrogen atoms do not participate in the Faradaic processes responsible for charge storage, the exact composition of TAQ within this compositional continuum bears no consequence on its electrochemical performance in a charge storage device, including batteries. Nevertheless, we note that the TAQ material we employed for battery studies has a n value around 0.985 based on the radical concentration.

Due to significant intramolecular and intermolecular $\pi-\pi$ interactions and hydrogen bonding, TAQ exhibits continuous electronic absorption from ultraviolet (UV) region to 1600 nm in its ultraviolet−visible−near-infrared (UV−vis−NIR) spectrum (Figure S7), resulting in an indirect optical bandgap of 0.75 eV (Figure 1d). This gap is smaller than those of most organic semiconductors.[21] The semiconducting nature of TAQ is further demonstrated by band structure calculations with projected density of states (pDOS), which show that TAQ has an indirect electronic bandgap of 0.459 eV (Figure 1e). Furthermore, the curvature of the bands along the high symmetry points in the reciprocal space suggests that the electrons have reasonable mobility. The pDOS diagram also reveals that carbon atoms contribute significantly to the valence band, indicating significant $\pi-\pi$ stacking interactions. Therefore, TAQ possesses promising charge transport properties, which is in stark contrast to typical OEMs with large bandgaps. Indeed, with a high electrical conductivity of 2.34×10^{-2} mS cm^{-1} (Figure S8), TAQ compares favorably to all other cathode materials for SIBs.[22,23]

Importantly, TAQ is insoluble in common organic solvents due to its robust intermolecular interactions, such that TAQ electrodes exhibit no dissolution after soaking in SIB electrolytes

https://doi.org/10.1021/jacs.4c17713
J. Am. Chem. Soc. XXXX, XXX, XXX−XXX

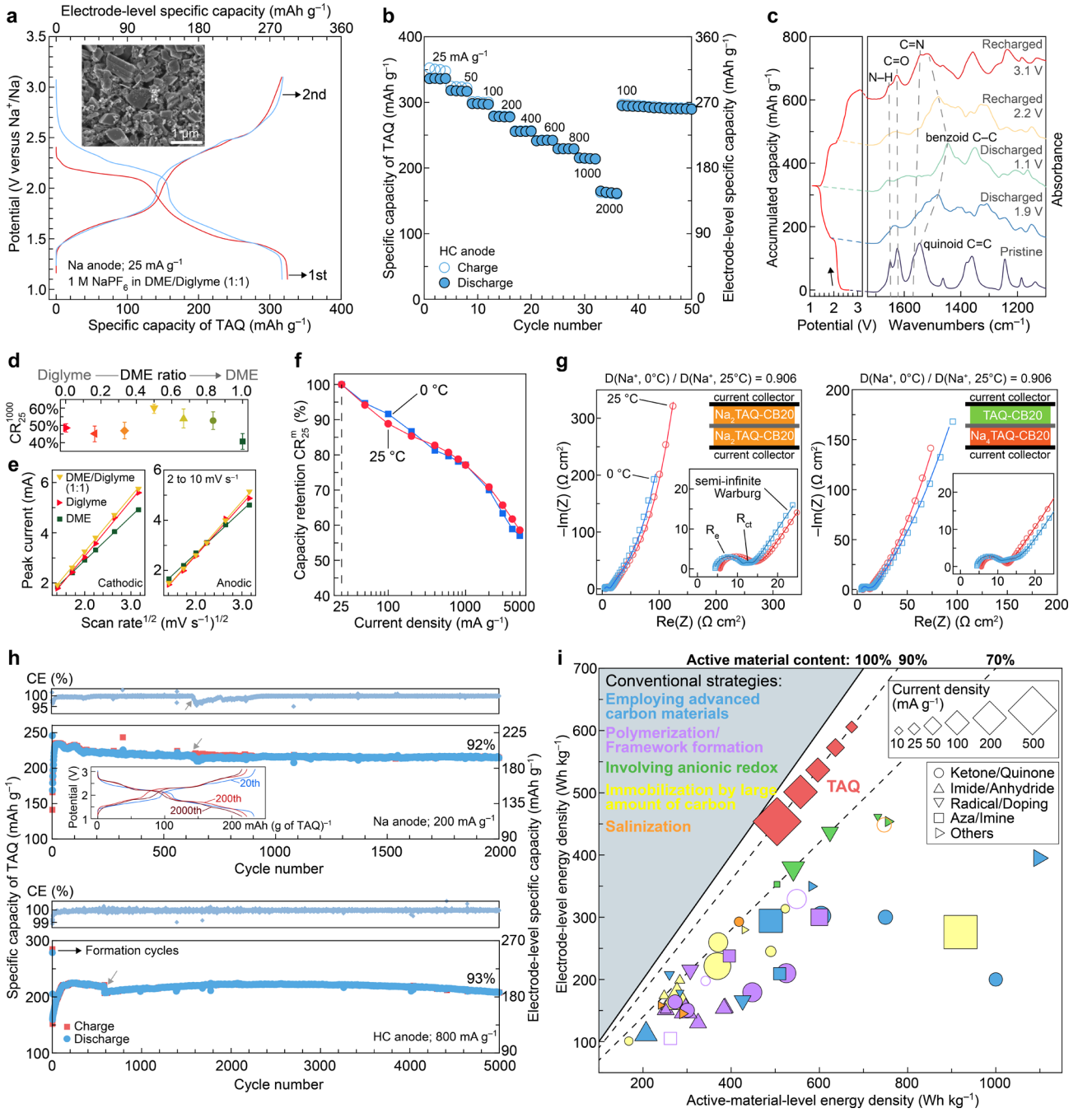

Figure 2. Battery performance of TAQ-CB cathodes.(a) Galvanostatic charge−discharge voltage profiles of a TAQ-CB5||Na cell using 1 M $NaPF_6$ in DME/Diglyme (1:1) as the electrolyte. The first discharge plateau shifts up by approximately 0.1 V in the second cycle (blue trace), whereas the second discharge plateau stays roughly at the same voltage. Inset shows an SEM image of a TAQ-CB5 electrode. (b) Rate capability study of a TAQ-CB5||HC (presodiated hard carbon) cell. (c) Ex situ ATR-FTIR spectra of TAQ-CB5 cathodes at different states of charge and discharge. The C═O, C═N, quinoid C═C, and benzene C−C bands are located at 1624, 1568, 1546, and 1447 cm^{-1}, respectively. (d) Rate capability comparisons of TAQ-CB5||Na cells using electrolytes with different ratios between DME and Diglyme. CR_{25}^{1000} results are average values based on 4∼5 half cells for each ratio. (e) The relationship between peak currents and scan rate plotted according to the Randles−Sevcik equation from CV measurements of half cells in DME, Diglyme, or DME/Diglyme (1:1) electrolytes. Solid lines represent the best linear fit. (f) Capacity retention CR_{25}^{m} ($25 \le m \le 5000$) of TAQ-CB20||Na cells at 25 °C (red) and 0 °C (blue). The use of 20 wt % CB ensures a good electron conduction in the electrode. (g) Nyquist plots of TAQ-CB20 symmetric cells at 25 °C (red) and 0 °C (blue) with two different states of charge: Na_2TAQ-CB20||Na_2TAQ-CB20 (left), and TAQ-CB20||Na_4TAQ-CB20 (right). Solid lines represent the best fit. (h) Cycling studies of a TAQ-CB5||Na cell at 200 mA g^{-1} (top), and a TAQ-CB5||HC cell at 800 mA g^{-1} (bottom). Insets show the evolution of voltage profiles during cycling. Gray arrows indicate disturbance of cycling studies due to unexpected power interruptions. (i) Electrode-level energy density of state-of-the-art organic cathodes and the TAQ-CB cathode versus their energy density at the active-material level. The sizes of scatters represent current densities, and the colors of scatters correspond to common strategies to solve dissolution and insulation problems of OEMs. Hollow scatters represent organic electrodes whose average discharge voltage is less than or equal to 1.5 V, which is not ideal for cathodes.

https://doi.org/10.1021/jacs.4c17713
J. Am. Chem. Soc. XXXX, XXX, XXX−XXX

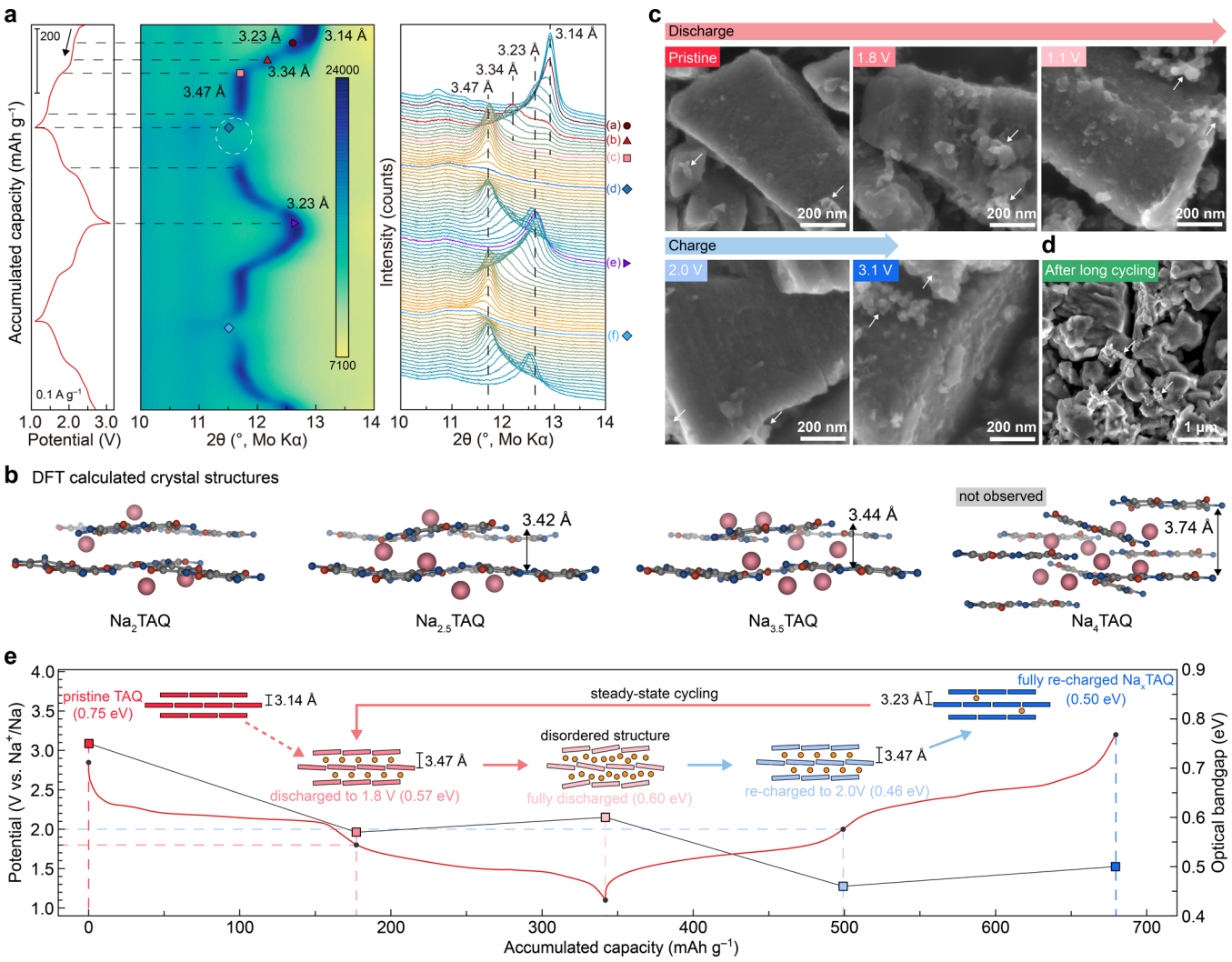

Figure 3. Structural changes of TAQ during discharge/charge. (a) *Operando* PXRD patterns of a TAQ||Na cell cycled at a current density of 100 mA g^{-1}. The voltage profile is shown on the left, and the individual PXRD patterns are shown on the right. (b) DFT-computed crystal structures of Na_2TAQ, $Na_{2.5}TAQ$, $Na_{3.5}TAQ$, and Na_4TAQ. (c) Ex situ SEM images of TAQ cathodes at different states of discharge/charge. (d) An SEM image of a TAQ cathode after long cycling. White arrows in c and d indicate carbon black particles and binder. (e) The first-cycle discharge/charge voltage profile of a representative TAQ-CB||Na cell at 25 mA g^{-1} with schematics of charge storage mechanism for TAQ. The ex situ elec bandgaps were prepared by discharging/charging to certain potentials. When discharged to 1.8 V, the composition corresponds roughly to $Na_{2.1}TAQ$; when recharged back to 2.0 V, the composition corresponds roughly to $Na_{1.8}TAQ$. The fully recharged state is denoted as Na_x TAQ, where x is between 0.1 and 0.3 calculated from the ICE values. Square symbols indicate the optical bandgap of TAQ cathodes at different states of discharge/charge.

for at least eight months (Figure S9). TAQ can accommodate up to four Na^+ ions per formula unit, through the reduction of carbonyl groups (Figure 1b), offering a theoretical specific capacity of 355 mAh g^{-1} per formula unit. The insolubility and desirable electron and ion transport features of TAQ enable the fabrication of TAQ-CBx cathodes (CB: carbon black; x indicates the weight percentage of CB), which consist as high as 90 wt % TAQ and as low as 5 wt % CB (Figure 2a inset).

Intrinsic Facile Na^+ Diffusion in TAQ Enables High Rate Capability. Na-ion half cells consisting of a TAQ-CB5 cathode, a metallic Na anode, and an ether-based electrolyte (1 M $NaPF_6$ in 1,2-dimethoxyethane (DME)/diethylene glycol dimethyl ether (Diglyme) (1:1))[24−26] were tested between 1.1 and 3.1 V (all potentials are referenced to the Na^+/Na couple unless otherwise noted), a potential window optimized for practical use.[20] The initial discharge/charge cycle of a half cell measured under a current density of 25 mA g^{-1} exhibited a voltage profile (Figure 2a) with two discharge steps centered around 2.15 and 1.5 V, which reveal roughly equal capacity. Each step contains two closely placed plateaus, suggesting four single-electron reduction processes per TAQ molecule, which are more clearly shown in the dQ/dV curve (Figure S10). Cyclic voltammograms (CV) (Figure S11) and dQ/dV curves both reveal three peaks at 1.7, 2.4, and 2.5 V during the charging process, corresponding to three plateaus in the charging voltage profile. The first plateau corresponds to a $2e^-$ oxidation, whereas the latter two correspond to two single-electron oxidations. The cell delivers a reversible discharge capacity of 325 mAh g^{-1} with an average discharge voltage of 2 V and a high initial Coulombic efficiency (ICE) of 97.8%. Notably, although a TAQ-CB20 cathode (with 75 wt % TAQ) delivers a higher active-material-level capacity of 337 mAh g^{-1} (Figure S12), the corresponding electrode-level capacity (i.e., based on the total mass of active material, CB, and binder), 253 mAh $g^{-1}_{electrode}$, is much lower than that of the TAQ-CB5 (with 90 wt % TAQ) cathode, 286 mAh $g^{-1}_{electrode}$. Moreover, the TAQ-CB5 electrode exhibits average reversible

https://doi.org/10.1021/jacs.4c17713
J. Am. Chem. Soc. XXXX, XXX, XXX−XXX

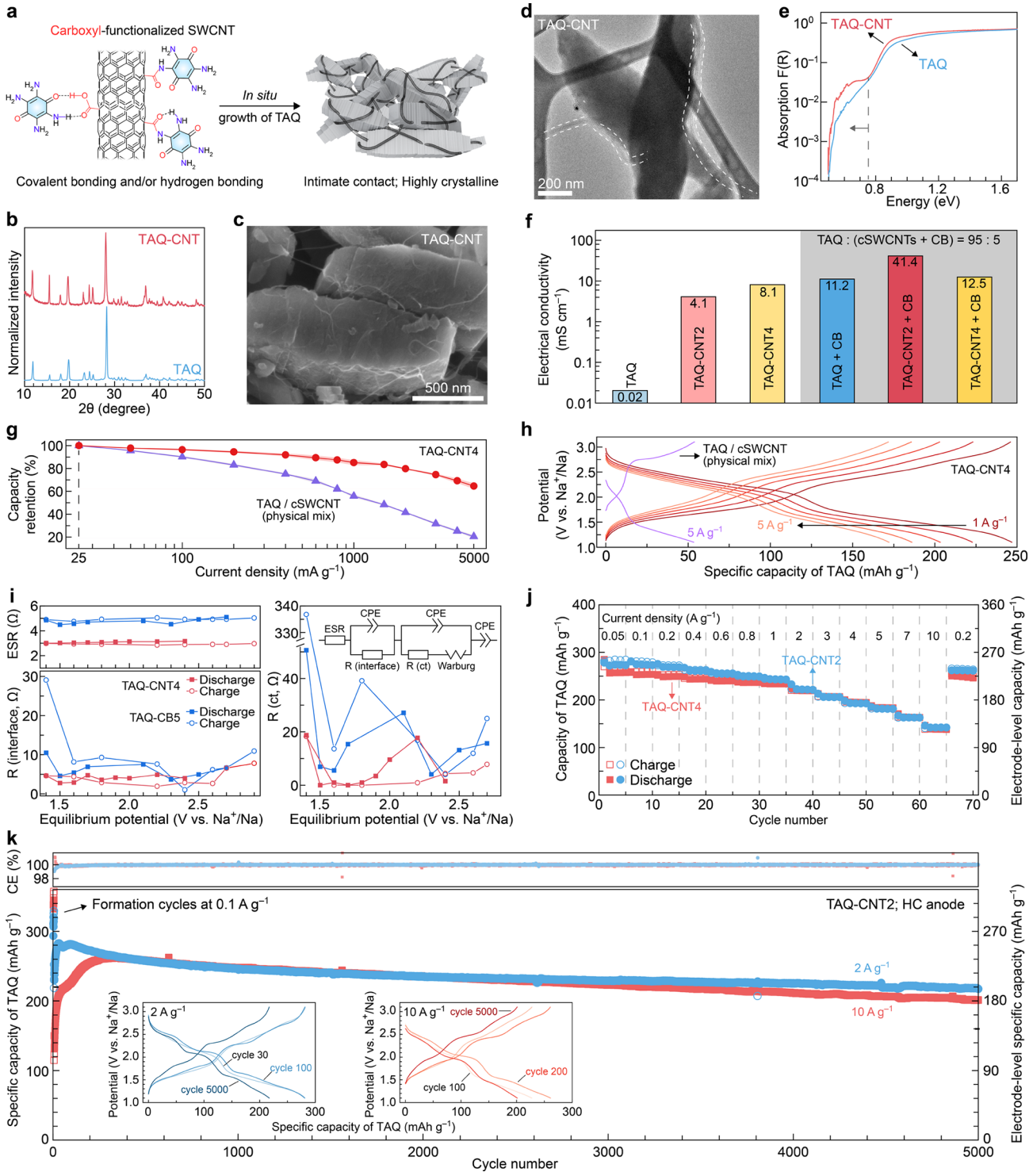

Figure 4. Characterization and battery performance of TAQ-cSWCNT composites. (a) In situ growth of TAQ with carboxyl-functionalized single-walled carbon nanotubes to form highly crystalline TAQ-CNT composites with intimate contact between TAQ crystallites and CNTs. (b) PXRD patterns of TAQ and TAQ-CNT4 composite. (c) An SEM image of TAQ-CNT composite. (d) A TEM image of TAQ-CNT composite. White dashed contours highlight cSWCNTs that wrap and interconnect TAQ crystals. (e) Diffuse reflectance UV−vis−NIR spectrum of TAQ-CNT composite, exhibiting enhanced electronic absorption below 0.75 eV (gray dashed line). (f) Electrical conductivities of TAQ, TAQ-CNT composites, and their mixtures with CB. (g) Comparison of CR_{25}^{m} ($50 \leq m \leq 5000$) for TAQ-CNT4 cathode and physically mixed TAQ/cSWCNT-based cathode. Both composites have the same amount of cSWCNTs. Color shaded areas indicate error bars based on two parallel cells. (h) Discharge/charge voltage profiles of the two cells in (g). (i) ESR, $R_{interface}$, and R_{ct} of TAQ-CB5 and TAQ-CNT4 based half cells at various equilibrium voltages during discharge and charge obtained by EIS studies. (j) Rate capability studies of TAQ-CNT2||HC and TAQ-CNT4||HC full cells under current densities ranging from 0.05 to 10 A g^{-1}. (k) Cycling studies of TAQ-CNT2||HC full cells at 2 and 10 A g^{-1}. Insets show selected voltage profiles during cycling.

discharge capacities of 298 and 214 mAh g^{-1} at higher current densities of 100 and 1000 mA g^{-1}, respectively (Figure 2b). The

https://doi.org/10.1021/jacs.4c17713
J. Am. Chem. Soc. XXXX, XXX, XXX−XXX

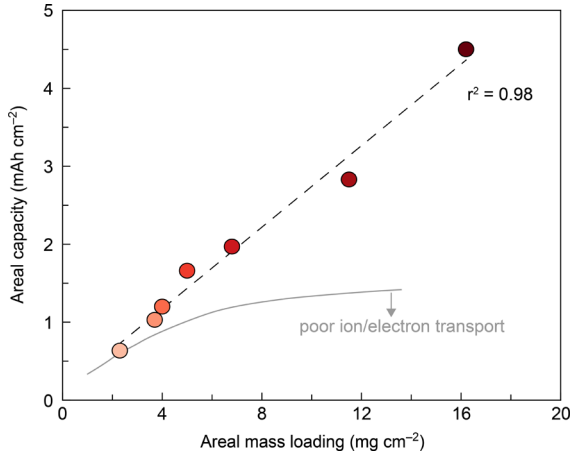

Figure 5. Dependence of areal capacity on TAQ mass loading of TAQ-CNT cathodes. The black dash line indicates the best linear fit. The gray line represents a typical dependence curve when ion and/or electron transport in electrodes are not good.

capacity restores to 296 mAh g^{-1} when the current density changed from 2 A g^{-1} back to 100 mA g^{-1}, demonstrating the high rate capability and stability of TAQ-CB5 cathodes.

Ex situ ATR-FTIR spectra of TAQ-CB5 electrodes at different states of discharge and charge during the initial cycle confirm that both C═O and C═N (from the imine tautomer) are redox centers, as their stretching bands gradually disappear during discharging and recover upon charging (Figure 2c and S13). This process is accompanied by the interconversion between the quinoid and the benzenoid structure, as evidenced by the shifting between the quinoid C═C stretching band and the benzene C−C stretching band. This spectroscopic evolution matches well with the redox mechanism of quinone-based compounds.[27,28]

Examination of TAQ-CB5 half-cells made with DME/diglyme electrolytes of varying composition provided insight into the intrinsic diffusion kinetics of Na^+ in TAQ (Figure S14). The capacity retentions at 1000 mA g^{-1} relative to 25 mA g^{-1} (denoted as CR_{25}^{1000}, where CR_n^m is defined as the capacity retention at m mA g^{-1} relative to n mA g^{-1}) in various electrolytes (Figure 2d) exhibit a volcano-like relationship with respect to the DME/diglyme ratio, with the DME/diglyme ratio of 1:1 leading to a peak CR_{25}^{1000} of 60%. Notably, such rate capability is normally achieved only when large amounts of carbon additives or surface carbon coatings are employed.[29−31] Further investigation of the electrolyte dependence using the Galvanostatic Intermittent Titration Technique (GITT) revealed apparent Na^+ diffusion coefficients (D_{Na^+}) in TAQ of approximately 10^{-10} cm^2 s^{-1} irrespective of the electrolyte composition when cycling at a low rate (25 mA g^{-1}) (Figure S15). This agrees with the nearly identical specific capacities obtained in these electrolytes at 25 mA g^{-1} (Figure S16). Interestingly, studies of the charge storage and ion transport under dynamic conditions using electrochemical impedance spectroscopy (EIS) reveal that TAQ-CB5||Na cells in DME and DME/Diglyme (1:1) electrolytes exhibit very similar charge transfer resistances (R_{ct}), which depend considerably on Na^+ intercalation kinetics (Figure S17 and Note S1). These values are significantly lower than those observed in the Diglyme electrolyte, suggesting that DME enhances the charge storage kinetics of TAQ. Surprisingly, ex situ SEM images reveal severe exfoliation and pulverization of TAQ crystallites for cycled TAQ-CB5 electrodes in diglyme electrolyte, whereas neither DME nor DME/diglyme (1:1) electrolytes cause morphological alteration in TAQ-CB5 electrodes (Figures S18−S20). Even though diglyme thus seems detrimental to the integrity of TAQ-CB, it is known as a good electrolyte for Na and hard carbon anodes.[32] As such, we opted for a 1 M $NaPF_6$ in DME/diglyme (1:1) as the optimized electrolyte that would balance the cathode and anode performance for TAQ-based SIBs.

To interrogate the mechanism giving rise to the high rate performance of TAQ, we carried out electrochemical kinetic studies through analyzing the currents from CV profiles of TAQ-CB5||Na cells using the power law relationship ($i = av^b$). We found that both cathodic and anodic peak currents are surface-controlled between scan rates of 0.1 and 2 mV s^{-1} (Figure S21 and Table S1), suggesting that the charge storage behaves as a quasi-2D process and is controlled by the surface of TAQ 2D layers at relatively low rates.[10] The b values deviate significantly from 1 (surface-controlled) between 2 and 10 mV s^{-1}, suggesting a considerably increased dependence of charge storage on Na^+ diffusion.[10] Indeed, Figure 2e shows the correlations between the cathodic or anodic peak currents and square root of scan rates between 2 and 10 mV s^{-1}, which fit well to a linear relationship for diffusion-controlled processes. Applying the Randles−Sevcik equation[33] yields estimated D_{Na^+} values of 8.5×10^{-9} and 7.6×10^{-9} cm^2 s^{-1} for Na^+ intercalation and deintercalation, respectively, at moderate to high rates in the DME/Diglyme (1:1) electrolyte, which are higher than both DME and Diglyme electrolytes (Table S2). These values rank among the highest for all cathode materials for SIBs,[34] indicating facile Na^+ diffusion within TAQ due to 2D diffusion pathways. More importantly, TAQ-CB20||Na cells exhibit very similar rate performance at 0 °C and 25 °C with high CR_{25}^{1000} values around 77% (Figures 2f and S22), implying almost temperature-independent rapid Na^+ diffusion. We further conducted EIS studies of symmetric cells[35−37] at two different states of charge, namely Na_2TAQ-CB20||Na_2TAQ-CB20 and TAQ-CB20||Na_4TAQ-CB20, under 0 °C and 25 °C to reveal solely the Na^+ diffusion kinetics in TAQ (see Experimental Procedures and Note S1). The ratios of D_{Na^+} (0 °C) over D_{Na^+} (25 °C) for the two states, calculated from the Warburg coefficients for semi-infinite diffusion within the bulk of TAQ particles, are both 90.6% (Figure 2g), suggesting a notably low Na^+ diffusion energy barrier. These results demonstrate that the facile 2D diffusion of Na^+ accounts for the intrinsic superior rate performance of TAQ-CB cathodes. The higher CR_{25}^{1000} for TAQ-CB20 cathodes than that for TAQ-CB5 cathodes also indicates that despite of the high electrical conductivity of TAQ, electron conduction is still the bottleneck for further improving the rate performance of TAQ-based cathodes.

A cycling study of a TAQ-CB5||Na cell at 200 mA g^{-1} (Figure 2h) reveals exceptional cycling stability with a capacity retention of 92% after 2000 cycles relative to the peak capacity. Importantly, this cell exhibits stable average discharge voltages very close to 2 V throughout the cycling, which shows essentially no drop relative to the value obtained at 25 mA g^{-1} (Figure S23). We note that the cell undergoes an activation process at the initial stage of cycling that is commonly observed in organic-rich cathode materials at moderate to high rates, which we attribute to the gradual improving of the electrolyte wetting of the porous electrodes during cycling.[6,7,22] Upon even more prolonged cycling, the TAQ-CB||HC full cell delivers an electrode-level cathode capacity of 187 mAh $g^{-1}_{electrode}$ and an energy density of 336 Wh $kg^{-1}_{electrode}$ after 5000 cycles (ca. 2700 h of cycling) at

https://doi.org/10.1021/jacs.4c17713
J. Am. Chem. Soc. XXXX, XXX, XXX−XXX

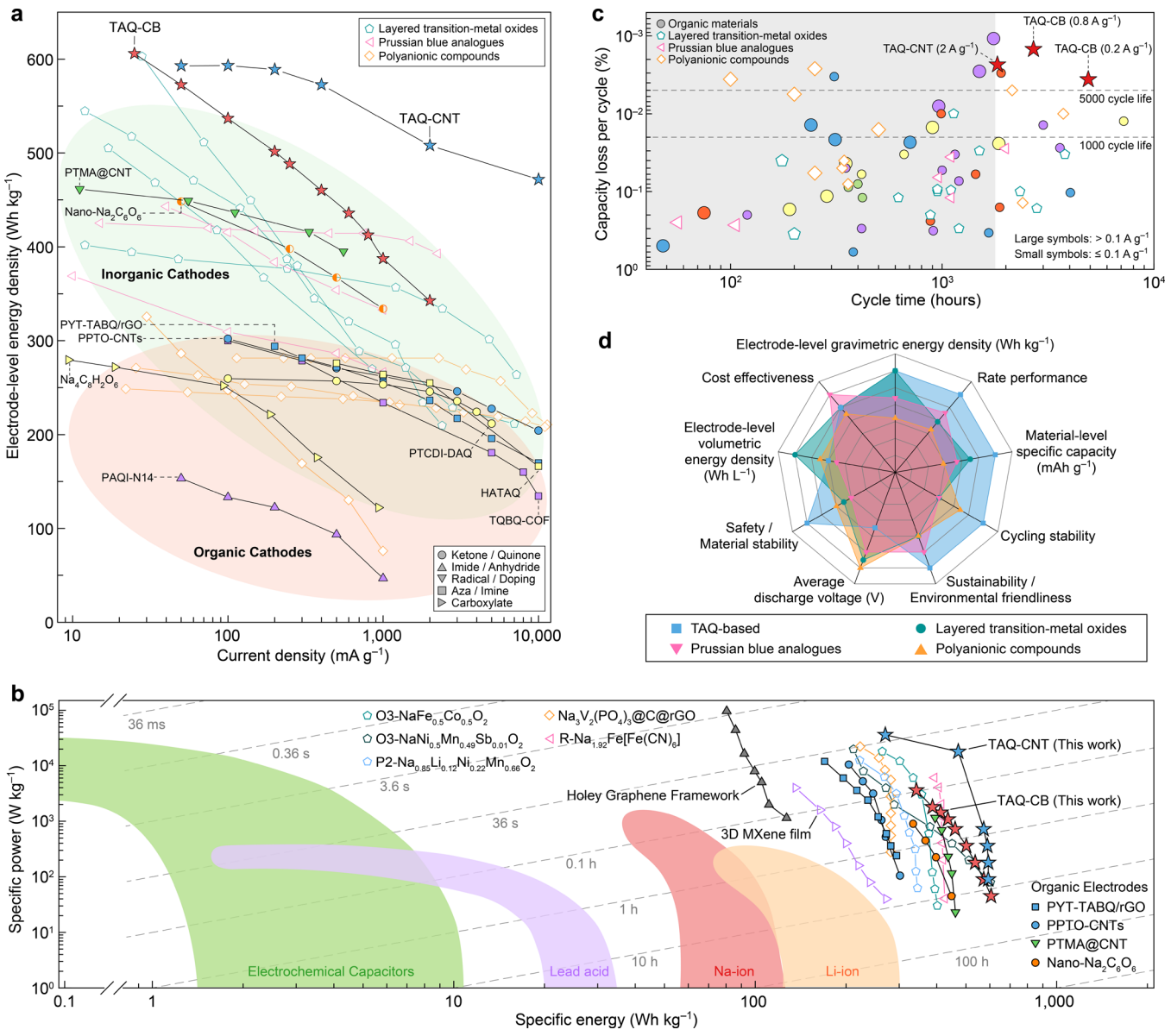

Figure 6. Benchmarking TAQ-based cathodes against state-of-the-art organic and inorganic SIB cathodes. (a) A comparison of the electrode-level gravimetric energy densities of TAQ-based cathodes with the best organic and inorganic cathodes at current densities ranging from 10 to 10,000 mA g^{-1}. Colors of scatters represent different strategies: yellow (immobilization by large amount of carbon); green (involving anionic redox); blue (employing advanced carbon materials); purple (polymerization/framework formation); orange (salinization). Half-hollow scatters indicate average discharge voltage less than or equal to 1.5 V. A complete comparison and the list of examples can be found in Source Data file, Figures S44 and S45. (b) Ragone plot of TAQ-based cathodes and selected inorganic and organic cathodes. State-of-the-art capacitive (Holey Graphene Framework) and pseudocapacitive (3D porous MXene film) materials are also presented for comparison. Colored areas represent performance metrics of commercial devices. (c) Capacity loss per cycle against cycle time of TAQ, organic, and inorganic cathode materials. The shadow area indicates cycle time of less than 1800 h. Same color codes for organic electrodes were applied as in (a). (d) SIB cathode performance assessments of TAQ, layered transition-metal oxides, Prussian blue analogues, and polyanionic compounds.

800 mA g^{-1}, corresponding to a decline of only 7.4% relative to the peak capacity. This slow capacity decay (0.00148% per cycle) indicates a projected lifespan of ~13,500 cycles until the capacity retention drops to 80%. We note that although the presodiation of anodes may prove challenging to scale in practical SIBs, this treatment significantly enhances the ICE of full cells, effectively reduces the irreversible capacity loss, and improves the cycling stability, thereby demonstrating its important role in the potential commercialization of SIBs.[38,39] Additionally, using presodiated anodes also solves the sodium deficiency problem of most OEMs.

Figure 2i compares the electrode-level energy density of TAQ with state-of-the-art OEMs. Although very few OEMs exhibit energy densities close to 1000 Wh kg^{-1} at the active-material level,[40,41] which is far beyond that of inorganic cathode materials, an energy density of 500 Wh $kg^{-1}_{electrode}$ at the electrode level has never been achieved even at ultralow current density of 10 mA g^{-1} due to the low active-material content (≤70 wt %). Increasing the active-material content in the electrode formulation normally leads to drastic drop in performance. On the contrary, TAQ-CB cathodes are capable of delivering electrode-level energy densities of 501.5 Wh $kg^{-1}_{electrode}$ at 200 mA g^{-1} and 606 Wh $kg^{-1}_{electrode}$ at 25 mA g^{-1}

https://doi.org/10.1021/jacs.4c17713
J. Am. Chem. Soc. XXXX, XXX, XXX−XXX

(see Source Data file in the Supporting Information), which are higher than all organic and most of inorganic cathode materials for SIBs. Such enhanced performance is attributed to TAQ's high theoretical capacity, inherent insolubility, and its low bandgap coupled with high electrical conductivity. TAQ-CB electrodes also reach a volumetric energy density of 723 Wh $L^{-1}_{electrode}$ based on the crystal-level density of approximately 2 g cm^{-3} and the electrode compact density of 1.1 g cm^{-3}, which is comparable to typical volumetric energy densities of Prussian blue analogues and polyanionic cathodes.[3,4]

Structural and Morphological Evolution of TAQ during Charge Storage. To reveal the structural origin of the intrinsic high rate capability of TAQ, we conducted *operando* powder X-ray diffraction (PXRD) measurements to understand the structural changes of TAQ during Na^+ intercalation and deintercalation. Upon discharging at 0.1 A g^{-1} during the first cycle, the main reflection peak at 3.14 Å, which translates to the interlayer distance of pristine TAQ, gradually disappears, while a new peak at 3.23 Å starts growing after the intercalation of approximately 0.4 Na^+ per TAQ molecule (Figure 3a, pattern (a)), suggesting the formation of an intermediate phase. The interlayer distance of this intermediate phase shifts continuously to around 3.34 Å (Figure 3a, pattern (b)) upon further intercalation of Na^+, which is followed by the phase transformation to the Na_2TAQ phase with an interlayer distance of 3.47 Å at the end of the first discharge plateau (~1.8 V; Figure 3a, pattern (c)). DFT calculations also confirm that Na^+ locates in-between molecular layers in Na_2TAQ (Figure 3b). Na_2TAQ continues to accommodate Na^+, converting to $Na_{3.5}$TAQ without major structural changes. Calculated crystal structures reveal interlayer distances of 3.42 Å for $Na_{2.5}$TAQ and 3.44 Å for $Na_{3.5}$TAQ, in good alignment with the experimental results. Surprisingly, the calculated crystal structure of Na_4TAQ reveals a drastic change of molecular packing from the layered stacking in $Na_{3.5}$TAQ to the offset stacking arrangement (Figures 3b and S24), leading to a significantly increased face-to-face distance between TAQ^{4-} of 3.74 Å with a predicted volume expansion larger than 20% relative to pristine TAQ. However, the calculated Na_4TAQ phase is not observed experimentally. Experimentally, Na_4TAQ has significantly weakened long-range ordering (Figure 3a, white circle, pattern (d)), likely due to the large crystal strain caused by deep intercalation of Na^+ and substantial electrostatic repulsion between TAQ^{4-}. Although the detailed structure of this highly disordered Na_4TAQ phase has proven difficult to probe, the broad reflection around 3.54 Å (see also pattern (f)) implies the preservation of the original layered structure. Therefore, we hypothesize that the ordered-to-disordered transformation during discharging from $Na_{3.5}$TAQ to Na_4TAQ prevents the calculated substantial alteration of the layered structure, leading to significantly less volume expansion. This reduced "swelling" observed experimentally is crucial to promote rate and cycling performance (Figure 3e). Crucially, the structural transformations that TAQ lattices undergo upon cycling are reversible: crystalline Na_2TAQ emerges again upon recharging (i.e., Na^+ deintercalation) through the first voltage plateau. Na_2TAQ further transforms into the recharged state (Figure 3a, pattern (e)), as the interlayer distance smoothly decreases from 3.47 to3.23 Å. The recharged state corresponds approximately to $Na_{0.3}$TAQ based on the ICE of ~93%, and is independent of current density (Figure S25). This minimally sodiated state may be preferred thermodynamically: the few remaining Na^+ ions may play a structural role by providing a slightly open interlayer distance and thus facilitating Na^+ intercalation and diffusion, evidenced by the smooth variation of interlayer distance between 3.23 and 3.47 Å and ~30% less volume change in subsequent cycles.

Operando PXRD measurements monitoring multiple Na^+ intercalation/deintercalation cycles at 0.2 A g^{-1} (Figure S25) further confirmed that the variation of the interlayer distance between 3.23 and 3.47 Å during cycling is highly reversible and stable. However, the disordered phase was almost invisible when the cell was discharged to 1.1 V because the capacity obtained at 0.2 A g^{-1}, 293 mAh g^{-1}, is lower than the value at 0.1 A g^{-1}, 316 mAh g^{-1}, and thus the intercalated Na^+ is not enough to induce the crystalline-to-disordered transition. The ability of TAQ to exhibit less structural alteration under higher current densities promotes its high rate capability. Remarkably, *operando* synchrotron wide-angle X-ray scattering measurements of a cell cycling at 1 A g^{-1} (Figure S26) reveal that the expansion of interlayer spacing to 3.47 Å is still facile under high rate operation, indicating that the diffusion of Na^+ in the 2D pathways between layers is rapid and pose no limitation to the rate performance of TAQ. As a result, the maximal change in interlayer distance of TAQ is only 7.4% during the steady-state cycling (Figure 3e), suggesting that the Na^+ storage in TAQ is accompanied by only a small degree of volume expansion, again in line with computational results.

Based on the experimental and computational data above, we propose that the origin of TAQ's high rate capability is 3-fold: (1) the in-plane hydrogen bonding network of TAQ provides structural integrity during Na^+ intercalation and deintercalation; (2) the vdW layered structure provides low-barrier 2D Na^+ diffusion pathways; (3) the favorable electronic structure of TAQ enables fast charge transport and transfer kinetics. Indeed, the microscopic morphology of TAQ crystallites remained almost unchanged upon discharging and recharging (Figure 3c), and no particle pulverization was observed even after long cycling (Figure 3d), a key feature required for long cycling. The subtle exfoliation along the cross-section of the TAQ crystallites and the roughening of the crystallite surface likely further improve the rate performance of TAQ cathodes.[42] Furthermore, ex situ DRUV−vis−NIR spectra of TAQ cathodes at different states of discharge/charge, obtained by discharging/charging to certain potentials, confirm that their bandgaps are all equal to or below 0.6 eV (Figures 3e and S27), significantly lower than the pristine state. Overall, the various formulations and structures of Na_xTAQ ($x = 0 \sim 4$) exhibit favorable electronic profiles for fast electronic charge transport regardless of the state of charge. This contrasts with other active cathode materials that undergo drastic shifts in electronic structures during cycling, and commonly exhibit inferior rate capability.[17]

In Situ Growth of TAQ-CNT Composites. With evidence at hand that the rate performance of TAQ cells may actually be gated by charge transport and not Na^+ diffusion, we sought to enhance the electrical conductivity of TAQ-based cathodes. Specifically, we focused on preparing composites of TAQ with carboxyl functionalized single-walled carbon nanotubes (cSWCNTs). In contrast to previous strategies that rely on $\pi-\pi$ interactions and normally require at least 20 wt % CNTs,[12] our composites contain as little as 2−4 wt % cSWCNTs, which is achieved through the in situ formation and growth of TAQ crystals wrapped with cSWCNTs (Figures 4a and S28). We denote these composites as TAQ-CNT*x*, where *x* represents *x* wt % cSWCNTs in the composite. We hypothesize that the carboxyl groups on the surface of cSWCNTs facilitate the growth of TAQ-CNT composite through hydrogen-bonding

https://doi.org/10.1021/jacs.4c17713
J. Am. Chem. Soc. XXXX, XXX, XXX−XXX

interaction and/or covalent bonding (i.e., amide formation) with amino groups of tetraamino-*p*-benzoquione (TAQ's precursor).[43] The TAQ-CNT composites exhibit high crystallinity (Figure 4b), and consist of TAQ microcrystals that are closely wrapped and interconnected by cSWCNTs (Figures 4c and S29). Transmission electron microscopy (TEM) images of TAQ-CNT composites further confirm that cSWCNTs attach firmly to the surface of TAQ crystallites, forming an intimate contact (Figures 4d and S30). In comparison, using non-functionalized SWCNTs yielded poorly crystalline heterogeneous composites comprising detached nanoparticles (Figure S31). This difference supports our hypothesis that the strong interaction between surface carboxyl groups and TAQ play a crucial role in the composite synthesis and integrity.

The Raman spectrum of TAQ-CNT composite (Figure S32) shows a red shift of the G band from 1597 cm^{-1} in the pristine cSWCNTs to 1587 cm^{-1} in the composite, indicating a strong electronic coupling between TAQ and cSWCNTs. This doping-like interaction markedly enhances the electronic absorption of the composite below the optical bandgap of pristine TAQ (Figure 4e) and leads to a smaller bandgap of approximately 0.5 eV (Figure S33), which favorably impacts electron conduction and charge transfer. The TAQ-CNT composites demonstrate a notable enhancement in electrical conductivity, reaching 8.1 mS cm^{-1} for TAQ-CNT4 (Figures 4f and S34a), an approximately 400-fold increase over neat TAQ.

Rate and Cycling Performance of TAQ-CNT Cathodes. Like TAQ-CB electrodes, TAQ-CNT electrodes consist of TAQ-CNT*x*, CB, and CMC/SBR, where the TAQ content is still 90 wt % and the total carbon (CB + cSWCNTs) content of 5 wt %. They exhibit compact and crack-free coatings even under high mass loadings (>10 mg cm^{-2}), likely due to the enhanced mechanical robustness brought by cSWCNTs (Figure S35). The TAQ-CNT4||Na cell exhibits a voltage profile very similar to a TAQ-CB||Na cell at 25 mA g^{-1} (Figure S36), but delivers an ICE of 100% and a lower polarization of 0.23 V compared to 0.31 V for the TAQ-CB||Na cell.

TAQ-CNT4 cathodes exhibit a capacity retention CR_{25}^{1000} reaching 88.3% (Figure 4g), and deliver a capacity of 246 mAh g^{-1} at 1 A g^{-1}, which corresponds to an electrode-level capacity of 221 mAh $g^{-1}_{electrode}$, an improved power performance relative to both TAQ-CB5 and TAQ-CB20 cathodes. Moreover, TAQ-CNT4 cathodes deliver 167 mAh $g^{-1}_{electrode}$ at 5 A g^{-1} with a CR_{25}^{5000} value of 67.0%. This rate capability is superior compared to a control, physically mixed TAQ/cSWCNT composite, which exhibits 48 mAh $g^{-1}_{electrode}$ at 5 A g^{-1} with a CR_{25}^{5000} value of only 20.4% (Figures 4g and S37). TAQ-CNT4 cathodes also exhibit essentially unchanged cell polarization of approximately 0.24 V when the current density is raised from 25 mA g^{-1} to 1 A g^{-1} (Figure 4h). The resulting round-trip efficiency (RTE) is around 90%, a value commonly observed for commercial lithium-ion batteries. Although the polarization increases to 0.396 V at 5 A g^{-1} and the RTE decreases slightly to 83%, such performance is substantially better than that of physically mixed TAQ/cSWCNT composites, which exhibit a severe polarization of 1.425 V at 5 A g^{-1} with a RTE of 49%.

To reveal the origin of improved rate performance of TAQ-CNT composites, we used GITT to determine D_{Na^+} in the TAQ-CNT4 cathode, which is only marginally higher than that in the TAQ-CB cathode (Figure S38). This confirmed that Na^+ diffusion does not limit the rate capability in TAQ-based electrodes. In contrast, EIS studies of TAQ-CNT4||Na cells at various states of discharge and charge (Figure 4i) reveal that the equivalent series resistances (ESR) decrease by more than 60% relative to TAQ-CB5||Na cells, as expected due to the higher conductivity of TAQ-CNT4 composites. Thus, the intimate contact between TAQ crystals and cSWCNTs significantly enhances the interfacial charge transport kinetics, leading to lower overall interfacial resistances ($R_{interface}$). Moreover, the charge transfer resistances (R_{ct}) of TAQ-CNT4||Na cells are also lower than TAQ-CB5||Na cells, indicating that cSWCNTs facilitate electron transfer kinetics of TAQ, likely through electronic coupling.

Surprisingly, TAQ-CNT2 cathodes exhibit higher capacity than TAQ-CNT4 cathodes at current densities from 0.1 to 10 A g^{-1} while using 50% less cSWCNTs (Figure 4j). Notably, a respectable electrode-level capacity of 132 mAh $g^{-1}_{electrode}$ is recorded for a TAQ-CNT2 electrode at a current density as high as 10 A g^{-1}, corresponding to a charging time of less than 1 min. The same cell recovers to a capacity of 266 mAh g^{-1} when the current density is reduced from 10 to 0.2 A g^{-1}, a negligible drop from the initial capacity of 269 mAh g^{-1} at 0.2 A g^{-1} (Figure 4j). To understand the underlying reason, we measured the electrical conductivity of the mixtures of TAQ or TAQ-CNT*x* composites with CB, which all have a total carbon (CB + cSWCNTs) content of 5 wt % to mimic the actual electrode formulation (Figures 4f and S34b). Indeed, the TAQ-CNT2/CB mixture exhibits the highest conductivity of 41.4 mS cm^{-1} compared with TAQ-CNT4/CB and TAQ/CB mixtures, which accounts for the improved performance of TAQ-CNT2 cathodes. Although containing more cSWCNTs, TAQ-CNT4/CB exhibit slightly more local aggregation of cSWCNTs compared to TAQ-CNT2/CB (Figure S29), leading to less efficient electron conduction. Stable repeated switching between ~300 mAh g^{-1} at 0.1 A g^{-1} and ~130 mAh g^{-1} at 10 A g^{-1} further showcases the ability of TAQ-CNT2 cathodes to tolerate abrupt power fluctuations and fulfill peak power requirements for most energy storage systems (Figure S39).

Cycling of a TAQ-CNT2||HC full cell at 2 A g^{-1} reveals an electrode-level cathode capacity of 196 mAh $g^{-1}_{electrode}$ after 5000 cycles, corresponding to a capacity retention of 94% relative to the initial capacity after formation cycles (Figure 4k). Remarkably, increasing the current density to 10 A g^{-1} showed almost no decrease of the peak capacity, meanwhile delivering an electrode-level cathode capacity of 181.2 mAh $g^{-1}_{electrode}$ after 5000 cycles. Importantly, TAQ-CNT2||HC full cells exhibit stabilized average discharge voltages of 1.97 V at 2 A g^{-1} and 1.94 V at 10 A g^{-1} (Figure S40), which are essentially unchanged relative to the value obtained at 25 mA g^{-1}. Although the average polarization of cells increases to 0.447 V at 10 A g^{-1}, the average RTE only drops slightly to 80%. An attempt to cycle a TAQ-CNT2||HC full cell at an ultrahigh current density of 20 A g^{-1} reveals a peak electrode-level discharge capacity of 135 mAh $g^{-1}_{electrode}$ after charging for less than 30 s (Figure S41). Although the power performance is limited by the rate capability of the anode, this cell still delivers electrode-level energy and power densities of 241 Wh $kg^{-1}_{electrode}$ and 31.6 kW $kg^{-1}_{electrode}$, respectively.

Effects of Mass Loadings on Full-Cell Performance. Increasing the areal mass loading of OEMs commonly leads to a drastic drop of their electrochemical performance. Consequently, organic cathodes for SIBs are generally tested at low mass loadings, commonly 1−2 mg cm^{-2}, which translate to inferior areal capacities. Figure 5 shows that TAQ-CNT electrodes exhibit almost loading-independent performance, as indicated by the linear relationship between areal mass loadings

https://doi.org/10.1021/jacs.4c17713
J. Am. Chem. Soc. XXXX, XXX, XXX−XXX

and areal capacities, whereas the areal capacities of other organic cathodes usually plateau out with increasing mass loadings due to poor electron and/or ion transport. Notably, an areal capacity of 4.5 mAh cm^{-2} is achieved in a TAQ-CNT||HC full cell with 16.2 mg cm^{-2} of TAQ and an N/P ratio of 1.2 (Figure S42), outperforming most organic cathodes. This cell also delivers a specific energy density of 182 Wh kg^{-1} based on the total mass of both cathode and anode, including conductive carbon and binder. This is superior to the most promising organic batteries with much lower mass loadings and is comparable with state-of-the-art inorganic full cells (Figure S43 and Table S3). Although the rate capability slightly reduces with increasing mass loading, 2.3 mAh cm^{-2} can still be achieved under a high areal current density of 3.2 mA cm^{-2}. We expect that electrode-level engineering, such as the optimization of cathode porosity and electrode architecture for better ion and charge transport, and cell-level engineering, such as using high-capacity anodes (e.g., phosphorus and tin),[44] would further improve the energy and power performance of TAQ-based sodium-ion full cells even at high mass loadings.[45,46]

Benchmarking TAQ-Based Cathodes against Other Cathode Material Classes for SIBs. Due to the low active material content in electrode formulations, organic cathodes for SIBs commonly exhibit less electrode-level gravimetric specific energies (≤400 Wh $kg^{-1}_{electrode}$) compared to their inorganic counterparts, which can exhibit specific energies exceeding 600 Wh $kg^{-1}_{electrode}$ (Figures 2g, 6a and S44, S45). Although a few OEMs exhibit specific energies between 400 and 500 Wh $kg^{-1}_{electrode}$, they either involve anion insertion,[47] or have an average discharge voltage that is not ideal as a cathode (i.e., ≤1.5 V).[41] They also often suffer from poor cycling stability due to severe dissolution.[48] Additionally, organic cathodes normally exhibit good rate capability only when considerable amount of conducting additives are used, so their electrode-level energy densities under high rates (e.g., ≥2 A g^{-1}) are still less satisfactory than those of inorganic cathodes. In contrast, TAQ-based cathodes, which contain 90 wt % of active material, show competitive electrode-level energy densities compared to state-of-the-art O3-type layered transition-metal oxides at low rates. They can deliver ∼30% or ∼100% more energy than inorganic cathodes at 2 and 10 A g^{-1}, respectively (Figure 6a). More relevantly, TAQ-based cathodes exhibit better power and energy performance compared to inorganic cathodes under the same charging/discharging time, while also significantly outperforming other organic cathodes. Specifically, TAQ-CNT cathodes exhibit a power density of 18 kW $kg^{-1}_{electrode}$ at 10 A g^{-1}, which is comparable to state-of-the-art capacitive and pseudocapacitive materials (Figure 6b), while delivering 2−6-fold higher energy density reaching 472 Wh $kg^{-1}_{electrode}$.

To compare the cycling stability of TAQ-based cathodes and other organic and inorganic SIB cathodes, we employ both capacity loss per cycle and total cycle time for a thorough evaluation. TAQ-based cathodes exhibit one of the lowest capacity loss per cycle, corresponding to projected cycle numbers far exceeding 5000 before the capacity drops to 80%. The reported cycle time of most inorganic and organic cathodes under more practical current densities (i.e., >0.1 A g^{-1}) is lower than 1800 h due to various reasons, such as chemical/structural instability and dissolution. Notably, TAQ-based cathodes can continuously cycle for more than 1800 h under a large range of current densities (Figure 6c).

CONCLUSIONS

Although organic cathodes generally show lower average discharge voltage compared to inorganic cathodes, TAQ-based cathodes and full cells exhibit highly competitive energy densities relative to commercially promising inorganic cathode technologies due to the high electrode-level specific capacity of TAQ-based electrodes (Figure 6d). As a result, TAQ-based SIB cathodes outperform $LiFePO_4$-based lithium-ion cathodes in both energy and power densities at the electrode level.[49] Furthermore, TAQ exhibits excellent material stability against air and moisture, superior rate performance, long lifespan, environmental friendliness, and sustainability (Figure 6d), a series of "soft" metrics that provide it with potential competitiveness as a cathode material for SIBs serving large-scale stationary energy storage applications, especially where high-quality power regulation is required.

In conclusion, we have demonstrated that TAQ cathodes for SIBs exhibit both high energy and power densities at the electrode level due to the combination of TAQ's low electronic bandgap with fast electron transport, facile 2D Na^+ diffusion pathways, and insolubility in electrolytes. Wrapping and interconnecting TAQ crystals with CNTs further improves the electrical conductivity of the cathode composite, leading to ultrahigh rate capability. Our results demonstrate the competitiveness of organic cathodes for SIBs and provide blueprints for future development of organic SIBs.

ASSOCIATED CONTENT

Supporting Information

The Supporting Information is available free of charge at https://pubs.acs.org/doi/10.1021/jacs.4c17713.

Source data for Figure 2i and Figure 6 (XLSX)

Experimental details, materials synthesis and characterization, battery fabrication, electrochemical characterizations, supplementary texts, figures, and tables (PDF)

AUTHOR INFORMATION

Corresponding Author

Mircea Dincă − *Department of Chemistry, Massachusetts Institute of Technology, Cambridge, Massachusetts 02139, United States;* orcid.org/0000-0002-1262-1264; Email: mdinca@mit.edu

Authors

Tianyang Chen − *Department of Chemistry, Massachusetts Institute of Technology, Cambridge, Massachusetts 02139, United States;* orcid.org/0000-0003-3142-8176

Jiande Wang − *Department of Chemistry, Massachusetts Institute of Technology, Cambridge, Massachusetts 02139, United States*

Bowen Tan − *Department of Chemistry, Massachusetts Institute of Technology, Cambridge, Massachusetts 02139, United States;* orcid.org/0000-0002-5166-1541

Kimberly J. Zhang − *Department of Chemistry, Massachusetts Institute of Technology, Cambridge, Massachusetts 02139, United States*

Harish Banda − *Department of Chemistry, Massachusetts Institute of Technology, Cambridge, Massachusetts 02139, United States*

Yugang Zhang − *Center for Functional Nanomaterials (CFN), Brookhaven National Laboratory, Upton, New York 11973, United States*

https://doi.org/10.1021/jacs.4c17713
J. Am. Chem. Soc. XXXX, XXX, XXX−XXX

Dong-Ha Kim − *Department of Chemistry, Massachusetts Institute of Technology, Cambridge, Massachusetts 02139, United States*

Complete contact information is available at: https://pubs.acs.org/10.1021/jacs.4c17713

Author Contributions

All authors have given approval to the final version of the manuscript. T.C. and J.W. contributed equally to this work.

Notes

The authors declare the following competing financial interest(s): M.D., H.B., T.C., J.W., and B.T. have pending patent and/or provisional patent applications covering the technology de-scribed here. The remaining authors declare no competing interests.

■ ACKNOWLEDGMENTS

This work was supported by Automobili Lamborghini S.p.A. This work was carried out in part through the use of MIT.nano's facilities. Cryo-EM specimens were prepared and imaged at the Automated Cryogenic Electron Microscopy Facility in MIT.nano on a Talos Arctica microscope, a gift from the Arnold and Mabel Beckman Foundation. This research used the resources of the Center for Functional Nanomaterials (CFN), the SMI beamline (12-ID) of the National Synchrotron Light Source II, a U.S. Department of Energy (DOE) Office of Science User Facility operated for the DOE Office of Science by Brookhaven National Laboratory under Contract No. DE-SC0012704.

■ REFERENCES

(1) Tarascon, J.-M. Na-ion versus Li-ion Batteries: Complementarity Rather than Competitiveness. *Joule* **2020**, *4* (8), 1616−1620.

(2) Zuo, W.; Innocenti, A.; Zarrabeitia, M.; Bresser, D.; Yang, Y.; Passerini, S. Layered Oxide Cathodes for Sodium-Ion Batteries: Storage Mechanism, Electrochemistry, and Techno-economics. *Acc. Chem. Res.* **2023**, *56* (3), 284−296.

(3) Peng, J.; Zhang, W.; Liu, Q.; Wang, J.; Chou, S.; Liu, H.; Dou, S. Prussian Blue Analogues for Sodium-Ion Batteries: Past, Present, and Future. *Adv. Mater.* **2022**, *34* (15), No. 2108384.

(4) Xu, C.; Zhao, J.; Yang, C.; Hu, Y.-S. Polyanionic Cathode Materials for Practical Na-Ion Batteries toward High Energy Density and Long Cycle Life. *ACS Cent. Sci.* **2023**, *9* (9), 1721−1736.

(5) Xu, S.; Dong, H.; Yang, D.; Wu, C.; Yao, Y.; Rui, X.; Chou, S.; Yu, Y. Promising Cathode Materials for Sodium-Ion Batteries from Lab to Application. *ACS Cent. Sci.* **2023**, *9* (11), 2012−2035.

(6) Zhang, H.; Gao, Y.; Liu, X. H.; Yang, Z.; He, X. X.; Li, L.; Qiao, Y.; Chen, W. H.; Zeng, R. H.; Wang, Y.; Chou, S. L. Organic Cathode Materials for Sodium-Ion Batteries: From Fundamental Research to Potential Commercial Application. *Adv. Funct. Mater.* **2021**, *32* (4), No. 2107718.

(7) Poizot, P.; Gaubicher, J.; Renault, S.; Dubois, L.; Liang, Y.; Yao, Y. Opportunities and Challenges for Organic Electrodes in Electrochemical Energy Storage. *Chem. Rev.* **2020**, *120* (14), 6490−6557.

(8) Lu, Y.; Chen, J. Prospects of Organic Electrode Materials for Practical Lithium Batteries. *Nat. Rev. Chem.* **2020**, *4* (3), 127−142.

(9) Kim, J.; Kim, Y.; Yoo, J.; Kwon, G.; Ko, Y.; Kang, K. Organic Batteries for a Greener Rechargeable World. *Nature Reviews Materials* **2023**, *8* (1), 54−70.

(10) Augustyn, V.; Come, J.; Lowe, M. A.; Kim, J. W.; Taberna, P. L.; Tolbert, S. H.; Abruna, H. D.; Simon, P.; Dunn, B. High-Rate Electrochemical Energy Storage Through Li^+ Intercalation Pseudocapacitance. *Nat. Mater.* **2013**, *12* (6), 518−522.

(11) Song, Z.; Qian, Y.; Zhang, T.; Otani, M.; Zhou, H. Poly(benzoquinonyl sulfide) as a High-Energy Organic Cathode for Rechargeable Li and Na Batteries. *Adv. Sci.* **2015**, *2* (9), No. 1500124.

(12) Shi, R.; Liu, L.; Lu, Y.; Li, Y.; Zheng, S.; Yan, Z.; Zhang, K.; Chen, J. In Situ Polymerized Conjugated Poly(pyrene-4,5,9,10-tetraone)/Carbon Nanotubes Composites for High-Performance Cathode of Sodium Batteries. *Adv. Energy Mater.* **2020**, *11* (6), No. 2002917.

(13) Shi, R.; Liu, L.; Lu, Y.; Wang, C.; Li, Y.; Li, L.; Yan, Z.; Chen, J. Nitrogen-Rich Covalent Organic Frameworks with Multiple Carbonyls for High-Performance Sodium Batteries. *Nat. Commun.* **2020**, *11* (1), 178.

(14) Wang, J.; Liu, X.; Jia, H.; Apostol, P.; Guo, X.; Lucaccioni, F.; Zhang, X.; Zhu, Q.; Morari, C.; Gohy, J.-F.; Vlad, A. A High-Voltage Organic Framework for High-Performance Na- and K-Ion Batteries. *ACS Energy Lett.* **2022**, *7*, 668−674.

(15) Wang, S.; Wang, L.; Zhu, Z.; Hu, Z.; Zhao, Q.; Chen, J. All Organic Sodium-Ion Batteries with $Na_4C_8H_2O_6$. *Angew. Chem., Int. Ed.* **2014**, *53* (23), 5892−5896.

(16) Chen, T.; Banda, H.; Yang, L.; Li, J.; Zhang, Y.; Parenti, R.; Dincă, M. High-Rate, High-Capacity Electrochemical Energy Storage in Hydrogen-Bonded Fused Aromatics. *Joule* **2023**, *7* (5), 986−1002.

(17) Chen, T.; Banda, H.; Wang, J.; Oppenheim, J. J.; Franceschi, A.; Dincă, M. A Layered Organic Cathode for High-Energy, Fast-Charging, and Long-Lasting Li-Ion Batteries. *ACS Cent. Sci.* **2024**, *10* (3), 569−578.

(18) Yao, Z.-F.; Wang, J.-Y.; Pei, J. Control of $\pi-\pi$ Stacking via Crystal Engineering in Organic Conjugated Small Molecule Crystals. *Cryst. Growth Des.* **2018**, *18* (1), 7−15.

(19) Kistenmacher, T. J.; Phillips, T. E.; Cowan, D. O. The Crystal Structure of the 1:1 Radical Cation-Radical Anion Salt of 2,2'-Bis-l,3-dithiole (TTF) and 7,7,8,8-Tetracyanoquinodimethane (TCNQ). *Acta Crystallogr. B* **1974**, *30* (3), 763−768.

(20) Li, Z.; Jia, Q.; Chen, Y.; Fan, K.; Zhang, C.; Zhang, G.; Xu, M.; Mao, M.; Ma, J.; Hu, W.; Wang, C. A Small Molecular Symmetric All-Organic Lithium-Ion Battery. *Angew. Chem., Int. Ed.* **2022**, *61* (33), No. e202207221.

(21) Costa, J. C. S.; Taveira, R. J. S.; Lima, C. F. R. A. C.; Mendes, A.; Santos, L. M. N. B. F. Optical Band Gaps of Organic Semiconductor Materials. *Opt. Mater.* **2016**, *58*, 51−60.

(22) Yin, X.; Sarkar, S.; Shi, S.; Huang, Q. A.; Zhao, H.; Yan, L.; Zhao, Y.; Zhang, J. Recent Progress in Advanced Organic Electrode Materials for Sodium-Ion Batteries: Synthesis, Mechanisms, Challenges and Perspectives. *Adv. Funct. Mater.* **2020**, *30* (11), No. 1908445.

(23) Novikova, S. A.; Larkovich, R. V.; Chekannikov, A. A.; Kulova, T. L.; Skundin, A. M.; Yaroslavtsev, A. B. Electrical Conductivity and Electrochemical Characteristics of $Na_3V_2(PO_4)_3$-Based NASICON-Type Materials. *Inorg. Mater.* **2018**, *54* (8), 794−804.

(24) Westman, K.; Dugas, R.; Jankowski, P.; Wieczorek, W.; Gachot, G.; Morcrette, M.; Irisarri, E.; Ponrouch, A.; Palacín, M. R.; Tarascon, J. M.; Johansson, P. Diglyme Based Electrolytes for Sodium-Ion Batteries. *ACS Appl. Energy Mater.* **2018**, *1* (6), 2671−2680.

(25) Tian, Z.; Zou, Y.; Liu, G.; Wang, Y.; Yin, J.; Ming, J.; Alshareef, H. N. Electrolyte Solvation Structure Design for Sodium Ion Batteries. *Adv. Sci.* **2022**, *9* (22), No. 2201207.

(26) Li, Y.; Wu, F.; Li, Y.; Liu, M.; Feng, X.; Bai, Y.; Wu, C. Ether-Based Electrolytes for Sodium Ion Batteries. *Chem. Soc. Rev.* **2022**, *51* (11), 4484−4536.

(27) Sieuw, L.; Jouhara, A.; Quarez, E.; Auger, C.; Gohy, J. F.; Poizot, P.; Vlad, A. A H-bond Stabilized Quinone Electrode Material for Li-Organic Batteries: the Strength of Weak Bonds. *Chem. Sci.* **2019**, *10* (2), 418−426.

(28) Jouhara, A.; Dupré, N.; Gaillot, A.-C.; Guyomard, D.; Dolhem, F.; Poizot, P. Raising the Redox Potential in Carboxyphenolate-Based Positive Organic Materials via Cation Substitution. *Nat. Commun.* **2018**, *9* (1), 4401.

(29) Xiong, W.; Huang, W.; Zhang, M.; Hu, P.; Cui, H.; Zhang, Q. Pillar[5]quinone−Carbon Nanocomposites as High-Capacity Cathodes for Sodium-Ion Batteries. *Chem. Mater.* **2019**, *31* (19), 8069−8075.

(30) Luo, W.; Allen, M.; Raju, V.; Ji, X. An Organic Pigment as a High-Performance Cathode for Sodium-Ion Batteries. *Adv. Energy Mater.* **2014**, *4* (15), No. 1400554.

(31) Song, J.; Park, S.; Kim, S.; Mathew, V.; Alfaruqi, M. H.; Jo, J.; Kim, J. Uniform Carbon Coated $Na_3V_2(PO_4)_2O_{2x}F_{3-2x}$ Nanoparticles for Sodium Ion Batteries as Cathode. *ACS Sustain. Chem. Eng.* **2019**, *7* (23), 18826−18834.
(32) Palanisamy, K.; Daboss, S.; Romer, J.; Schäfer, D.; Rohnke, M.; Flowers, J. K.; Fuchs, S.; Stein, H. S.; Fichtner, M.; Kranz, C. Microscopic and Spectroscopic Analysis of the Solid Electrolyte Interphase at Hard Carbon Composite Anodes in 1 M $NaPF_6$/Diglyme. *Batteries Supercaps* **2024**, *7* (3), No. e202300482.
(33) Kim, T.; Choi, W.; Shin, H.-C.; Choi, J.-Y.; Kim, J. M.; Park, M.-S.; Yoon, W.-S. Applications of Voltammetry in Lithium Ion Battery Research. *J. Electrochem. Sci. Technol.* **2020**, *11* (1), 14−25.
(34) Wang, Q.; Jiang, K.; Feng, Y.; Chu, S.; Zhang, X.; Wang, P.; Guo, S.; Zhou, H. P2-Type Layered $Na_{0.75}Ni_{1/3}Ru_{1/6}Mn_{1/2}O_2$ Cathode Material with Excellent Rate Performance for Sodium-Ion Batteries. *ACS Appl. Mater. Interfaces* **2020**, *12* (35), 39056−39062.
(35) Momma, T.; Yokoshima, T.; Nara, H.; Gima, Y.; Osaka, T. Distinction of Impedance Responses of Li-Ion Batteries for Individual Electrodes using Symmetric Cells. *Electrochim. Acta* **2014**, *131*, 195−201.
(36) Ogihara, N.; Itou, Y.; Sasaki, T.; Takeuchi, Y. Impedance Spectroscopy Characterization of Porous Electrodes under Different Electrode Thickness Using a Symmetric Cell for High-Performance Lithium-Ion Batteries. *J. Phys. Chem. C* **2015**, *119* (9), 4612−4619.
(37) Yoon, S.-B.; Jegal, J.-P.; Roh, K. C.; Kim, K.-B. Electrochemical Impedance Spectroscopic Investigation of Sodium Ion Diffusion in MnO_2 Using a Constant Phase Element Active in Desired Frequency Ranges. *J. Electrochem. Soc.* **2014**, *161* (4), H207.
(38) Mu, J.-J.; Liu, Z.-M.; Lai, Q.-S.; Wang, D.; Gao, X.-W.; Yang, D.-R.; Chen, H.; Luo, W.-B. An Industrial Pathway to Emerging Presodiation Strategies for Increasing the Reversible Ions in Sodium-Ion Batteries and Capacitors. *Energy Mater.* **2022**, *2* (6), 200043.
(39) Zhang, M.; Li, Y.; Wu, F.; Bai, Y.; Wu, C. Boost Sodium-Ion Batteries to Commercialization: Strategies to Enhance Initial Coulombic Efficiency of Hard Carbon Anode. *Nano Energy* **2021**, *82*, No. 105738.
(40) Kuan, H.-C.; Luu, N. T. H.; Ivanov, A. S.; Chen, T.-H.; Popovs, I.; Lee, J.-C.; Kaveevivitchai, W. A Nitrogen- and Carbonyl-Rich Conjugated Small-Molecule Organic Cathode for High-Performance Sodium-Ion Batteries. *J. Mater. Chem. A* **2022**, *10* (30), 16249−16257.
(41) Lee, M.; Hong, J.; Lopez, J.; Sun, Y.; Feng, D.; Lim, K.; Chueh, W. C.; Toney, M. F.; Cui, Y.; Bao, Z. High-Performance Sodium−Organic Battery by Realizing Four-Sodium Storage in Disodium Rhodizonate. *Nat. Energy* **2017**, *2* (11), 861−868.
(42) Lukatskaya, M. R.; Mashtalir, O.; Ren, C. E.; Dall'Agnese, Y.; Rozier, P.; Taberna, P. L.; Naguib, M.; Simon, P.; Barsoum, M. W.; Gogotsi, Y. Cation Intercalation and High Volumetric Capacitance of Two-Dimensional Titanium Carbide. *Science* **2013**, *341* (6153), 1502−1505.
(43) Acosta-Guzmán, P.; Ojeda-Porras, A.; Gamba-Sánchez, D. Contemporary Approaches for Amide Bond Formation. *Adv. Synth. Catal.* **2023**, *365* (24), 4359−4391.
(44) Chang, G.; Zhao, Y.; Dong, L.; Wilkinson, D. P.; Zhang, L.; Shao, Q.; Yan, W.; Sun, X.; Zhang, J. A Review of Phosphorus and Phosphides as Anode Materials for Advanced Sodium-Ion Batteries. *J. Mater. Chem. A* **2020**, *8* (10), 4996−5048.
(45) Sun, H.; Mei, L.; Liang, J.; Zhao, Z.; Lee, C.; Fei, H.; Ding, M.; Lau, J.; Li, M.; Wang, C.; Xu, X.; Hao, G.; Papandrea, B.; Shakir, I.; Dunn, B.; Huang, Y.; Duan, X. Three-Dimensional Holey-Graphene/Niobia Composite Architectures for Ultrahigh-Rate Energy Storage. *Science* **2017**, *356* (6338), 599−604.
(46) Gallagher, K. G.; Trask, S. E.; Bauer, C.; Woehrle, T.; Lux, S. F.; Tschech, M.; Lamp, P.; Polzin, B. J.; Ha, S.; Long, B.; Wu, Q.; Lu, W.; Dees, D. W.; Jansen, A. N. Optimizing Areal Capacities through Understanding the Limitations of Lithium-Ion Electrodes. *J. Electrochem. Soc.* **2016**, *163* (2), A138.
(47) Gannett, C. N.; Peterson, B. M.; Melecio-Zambrano, L.; Trainor, C. Q.; Fors, B. P.; Abruña, H. D. Performance Optimization and Fast Rate Capabilities of Novel Polymer Cathode Materials through Balanced Electronic and Ionic Transport. *J. Mater. Chem. A* **2021**, *9* (9), 5657−5663.
(48) Liu, X.; Ye, Z. Nitroaromatics as High-Energy Organic Cathode Materials for Rechargeable Alkali-Ion (Li^+, Na^+, and K^+) Batteries. *Adv. Energy Mater.* **2020**, *11* (4), No. 2003281.
(49) Rudola, A.; Sayers, R.; Wright, C. J.; Barker, J. Opportunities for Moderate-Range Electric Vehicles using Sustainable Sodium-Ion Batteries. *Nat. Energy* **2023**, *8* (3), 215−218.

https://doi.org/10.1021/jacs.4c17713
J. Am. Chem. Soc. XXXX, XXX, XXX−XXX